Self-chaperoning of the Type III Secretion System Needle Tip Proteins IpaD and BipD*[S]

Steven Johnson[‡§1,2], **Pietro Roversi**[‡1,3], **Marianela Espina**[¶], **Andrew Olive**[¶], **Janet E. Deane**[‡4], **Susan Birket**[¶], **Terry Field**[||], **William D. Picking**[¶5], **Ariel J. Blocker**[§6], **Edouard E. Galyov**[||], **Wendy L. Picking**[¶], and **Susan M. Lea**[‡§7]

From the ‡*Laboratory of Molecular Biophysics, Department of Biochemistry, University of Oxford, South Parks Road, Oxford, Oxon OX1 3QU, United Kingdom, the* §*Sir William Dunn School of Pathology, University of Oxford, OX1 3RE Oxford, United Kingdom, the* ¶*Department of Molecular Biosciences, University of Kansas, Lawrence, Kansas 66045, and the* ||*Division of Microbiology, Institute for Animal Health, Compton Laboratory, Berkshire RG20 7NN, United Kingdom*

Bacteria expressing type III secretion systems (T3SS) have been responsible for the deaths of millions worldwide, acting as key virulence elements in diseases ranging from plague to typhoid fever. The T3SS is composed of a basal body, which traverses both bacterial membranes, and an external needle through which effector proteins are secreted. We report multiple crystal structures of two proteins that sit at the tip of the needle and are essential for virulence: IpaD from *Shigella flexneri* and BipD from *Burkholderia pseudomallei*. The structures reveal that the N-terminal domains of the molecules are intramolecular chaperones that prevent premature oligomerization, as well as sharing structural homology with proteins involved in eukaryotic actin rearrangement. Crystal packing has allowed us to construct a model for the tip complex that is supported by mutations designed using the structure.

Currently, more than 1 million people die *per annum* as a result of T3SS[8]-expressing enteropathogenic bacteria such as *Shigella flexneri*, the causative agent of human bacillary dysen-

tery (1). The T3SS is composed of a basal body, which traverses both bacterial membranes and an external needle through which effector proteins are secreted (2). During infection, secretion is activated by contact of the tip of the needle complex with host cells (3) resulting in formation of a pore in the host cell membrane that is thought to be contiguous with the needle (4). Other effector proteins are injected through this apparatus directly into the host cell cytoplasm (for a review, see Ref. 5). T3SS-expressing bacteria can be classified into distinct phylogenetic families, both at the sequence level and by their general mechanism of infection (6). The Inv-Mxi-Spa family express T3SS, which trigger uptake of bacteria by non-phagocytic cells and includes *S. flexneri* and *Burkholderia pseudomallei*.

Shigella spp. cause bacillary dysentery by invasion of the colonic epithelium (7). Of the *S. flexneri* T3SS effector proteins, IpaB, IpaC, and IpaD are essential for invasion (8). IpaB and IpaC have been demonstrated to insert into the host cell membrane, thereby forming the translocation pore (4). Bacteria lacking IpaD are not only incapable of pore insertion and invasion but also demonstrate impaired effector secretion control (9). IpaD was originally proposed to form a plug in the T3SS with IpaB (3), while more recent data have demonstrated that its role is more complex (9). Deletions within the N-terminal third of the molecule do not affect invasion of host cells by the bacteria, although the insertion of IpaB/IpaC into membranes is slightly impaired. However, even short deletions (5 residues) in the C terminus of IpaD completely abolish the invasive phenotype and pore insertion (9). These observations led us to suggest that IpaD may play a role in regulating insertion of the IpaB/IpaC translocon pore from the tip of the *S. flexneri* needle (9, 10). Our recent data conclusively demonstrate IpaD is at the tip of intact T3SS embedded in the bacterial membranes and on isolated needles even prior to secretion induction (11). Similarly, the functional homologue in *Yersinia pestis*, LcrV, has also recently been localized to the tip of the needle and is required for pore formation (12).

B. pseudomallei causes melioidosis in humans, a disease endemic in Southeast Asia and Northern Australia. This disease presents in a variety of ways from subacute and chronic suppurative infections to a rapidly fatal septicemia (13). *B. pseudomallei* infection is dependent on a T3SS, which contains clear homologues of IpaB/C/D termed BipB/C/D (14). The overall sequence identity between IpaD and BipD is only 26%,
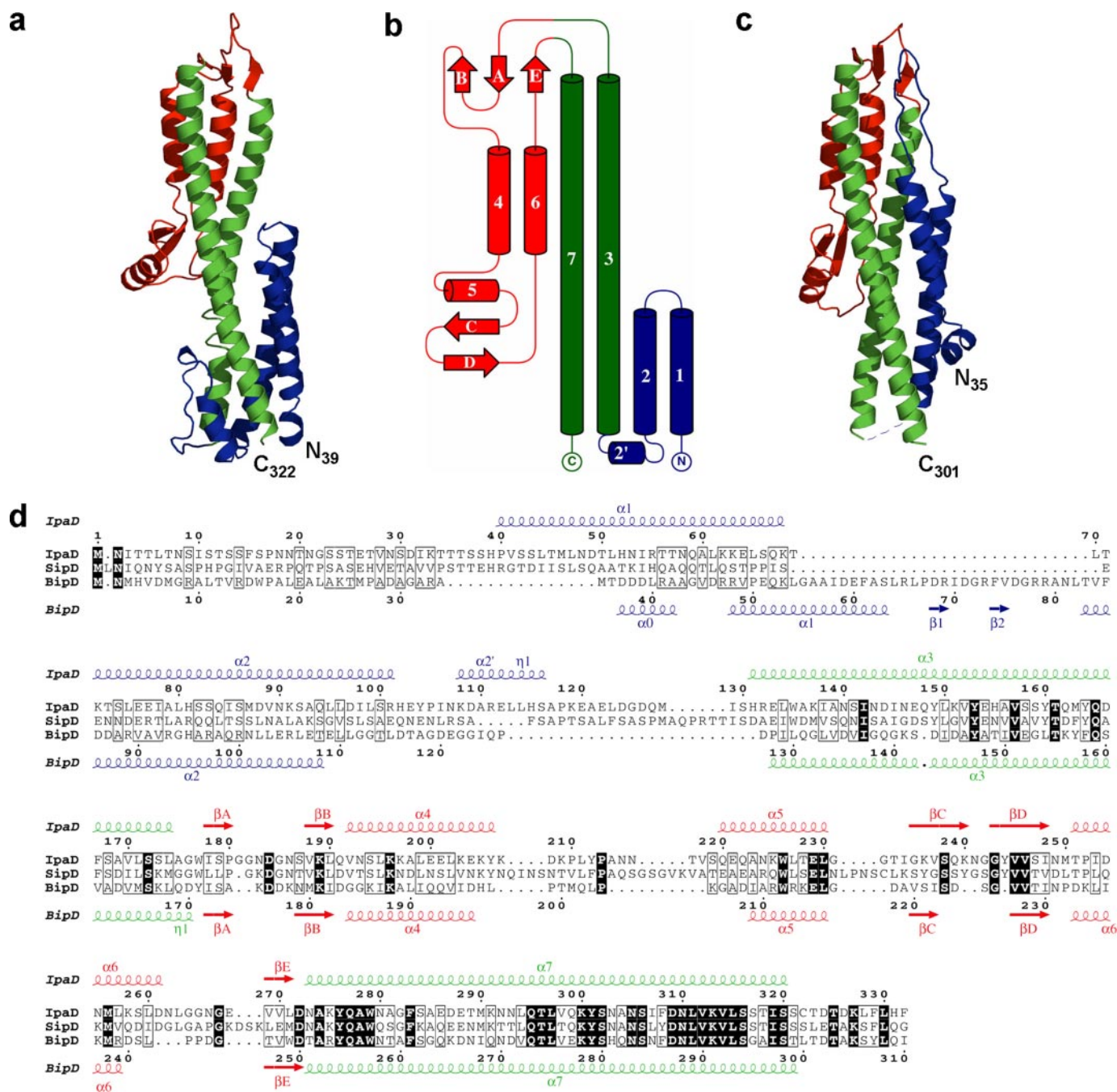
FIGURE 1. **Crystal structures of IpaD and BipD.** *a, ribbon diagram* of the structure of IpaD (residues 39–322) colored by domain: N-domain (*blue*), central coiled-coil (*green*), C-domain (*red*). *b*, topology diagram of IpaD, colored as in *a*. *c*, structure of BipD (residues 35–111 and 127–301) colored as in *a*. All figures were produced using PyMOL (26). *d*, structure based sequence alignment of IpaD, SipD, and BipD using the ESPript server (30), colored according to residue conservation. Secondary structure elements of IpaD and BipD are shown above and below the alignment respectively. The *Salmonella enterica typhimurium* homologue SipD is more closely related to IpaD.

however, with most of the conserved residues residing in the C-terminal quarter of the sequence (Fig. 1).

We have recently determined the crystal structure of MxiH, the *S. flexneri* needle subunit, and assembled a molecular model of a T3SS needle by docking it into our 16 Å electron microscopy reconstruction of the *S. flexneri* needle (15, 16). As part of an ongoing study into the interactions of the T3SS with host cells, we have now crystallized and determined the structures of IpaD and BipD. Their three-dimensional structures, in conjunction with the structure of the MxiH needle and other tip

proteins such as LcrV (17), significantly increase our understanding of these complex biological machines.

MATERIALS AND METHODS

IpaD Crystal Structure Determination—Protein preparation and crystallization were described previously (18). The positions of 8 selenium atoms in the SeMet-labeled crystal form 4 (CF-4) were obtained by analyzing the measured anomalous differences using SHELXC/D (19) within the suite of computer programs autoSHARP (20). Initial phases were calculated with

TABLE 1

IpaD and BipD refinements statistics (program Buster-TNT)

Values for the highest resolution shell are given in parentheses.

Crystal	IpaD CF-1	IpaD CF-2	IpaD CF-4	BipD CF-1	BipD CF-2
Space group (Z)	$P2_12_12_1$ (8)	C2 (8)	C2 (8)	$P2_12_12$ (8)	C222 (8)
Cell parameters (Å)	$a = 55.9$, $b = 100.7$, $c = 112.0$	$a = 77.9$, $b = 91.5$, $c = 54.9$ $\beta = 96.4°$	$a = 137.8$, $b = 44.5$, $c = 100.3$ $\beta = 108.0°$	$a = 136.5$, $b = 89.8$, $c = 50.2$	$a = 104.0$, $b = 122.8$, $c = 49.2$
Resolution range (Å)	20.0-3.0 (3.1-3.0)	15.0-2.1 (2.2-2.1)	34.0-3.1 (3.3-3.1)	54.0-2.7 (2.9-2.7)	40.0-2.6 (2.8-2.6)
Unique reflections	12,157	22,218	9791	17,569	10,013
R (%)	0.237 (0.276)	0.190 (0.208)	0.263 (0.262)	0.218 (0.253)	0.206 (0.226)
R_{work} (%)	0.235 (0.271)	0.189 (0.207)	0.262 (0.268)	0.216 (0.251)	0.203 (0.224)
R_{free} (%)	0.271 (0.376)	0.216 (0.229)	0.276 (0.308)	0.259 (0.288)	0.245 (0.263)
r.m.s.d. bond lengths (Å)	0.002	0.007	0.005	0.003	0.005
r.m.s.d. bond angles (°)	0.59	1.22	0.60	0.78	0.42
Residues modeled (range)	A, B: 39–322	A: 144–314 B: 133–319	A: 128–177; 192–260; 273–320 B: 123–180; 188–263; 273–320	A: 35–111; 127–301 B: 35–111; 125–301	A: 34–111; 125–302
Waters modeled	21	208	8	44	50
Non-protein molecules	1 glycerol			1 citrate, 2 boric acid	
Protein Data Bank identifier	2j0o	2j0n	2jaa	2j9t	2ixr

the program SHARP (21) using the data from a native crystal and a multiwavelength anomalous dispersion data set from a SeMet derivative (three peak wavelength data sets and one remote wavelength data set). Analysis of the Log-likelihood gradient maps in SHARP revealed two more selenium sites, which were added to the phasing job and the SHARP phases were extended to 2.8 Å by solvent flattening in SOLOMON. See supplemental Table 1 for phasing statistics. Non-crystallographic symmetry (NCS) 2-fold averaging was carried out in RESOLVE (22) using the positions of the selenium to calculate an initial NCS operator. An initial helical model was built in the program CCP4-ARP/wARP-HelixBuild (23) using these phases, and side chains were remodelled to the IpaD sequence in Xfit (24), using the selenium positions as sequence markers. The 2-fold NCS operator was used to group the helices into two monomers, and two copies of one such monomer were then located by molecular replacement in both CF-1 and CF-2 (18) using CCP4-PHASER (23). 6-Fold cross-crystal averaging between the three crystal forms was performed using CCP4-DMMULTI (23) and produced a 2.1 Å map in CF-2, which enabled automated building in CCP4-ARP/wARP (270 residues built, of which 227 were docked into sequence). Alternate cycles of refinement using Buster-TNT (25) and manual rebuilding in Xfit led to the final model in CF-2 of residues 144–314 for copy A and 133–319 for copy B. The complete model from CF-2 was used to guide manual building of models in CF-4 (residues 128–177, 192–260, and 273–320 in copy A and 123–180, 188–263, and 273–320 in copy B) with a combination of molecular replacement phases and density modification in DM and DMMULTI. Finally, the N-terminal domain of IpaD (residues 39–130) was built in CF-1 using Buster-TNT to model the missing atoms during the initial stages of refinement of the incomplete structure. Once the residues defining helices $\alpha1$ and $\alpha2$ were built, this model was used to phase the anomalous differences of a mercury-soaked CF-1 crystal in CCP4-FFT (23), and locate 2 Hg ions, which in turn were used to improve the CF-1 phases in SHARP, followed by solvent-flattening in SOLOMON to 2.8 Å. The SHARP-SOLOMON phases were combined with the Buster-TNT phases, and 4-fold averaging between CF-1 and CF-2 was repeated, again using DMMULTI. These maps allowed manual building of the final model for CF-1 of residues 39–322 for copy A and for copy B. All pictures were generated using PyMOL (26).

BipD Crystal Structure Determination—Protein preparation and crystallization were described previously (27). The positions of 2 platinum ions were obtained by analyzing the anomalous differences of a K_2PtCl_4 soaked derivative of the $P2_12_12$ crystal form using SHELXC/D (19) in autoSHARP (20). Initial 3.0 Å phases were calculated with the program SHARP (21) using the single isomorphous replacement with anomalous scattering (SIRAS) method with data from a native crystal and the platinum derivative. After addition of the data for a SeMet derivative crystal, analysis of the Log-likelihood gradient maps in SHARP revealed 10 selenium sites; SOLVE/RESOLVE (22) extended these multiple isomorphous replacement with anomalous scattering (MIRAS) SHARP phases to 2.7 Å and autobuilt and docked in sequence BipD residues 49–69, 77–95, 99–110, 128–166, 180–197, 201–212, 232–238, and 243–301 in at least one of the two independent monomers. The autodocked sequence and the selenium positions guided the determination of the NCS 2-fold operator relating chains A and B, and the NCS was then used to fill the gaps in the autobuilt model for either chain. Finally, iterative cycles of manual building in Xfit (24) and Buster-TNT refinement with soft NCS restraints yielded a model for residues 35–110 and 128–301 for both BipD molecules A and B. The $P2_12_12$ model was used to solve the C222 crystal form by molecular replacement with the program CCP4-PHASER (23).

Structure Superposition—All structure superpositions were carried out using the program CCP4-lsqkab (23) as follows: IpaD onto IpaD, BipD and MxiH using superpose topology; IpaD onto FliS (1ORJ-A), YscE (1ZW0-A), α-catenin (1DOV-A), vinculin (1RKC-A), and talin (1SJ7-A) using the residue mapping as defined by the DALI server (28).

Sequence Alignment—IpaD was aligned with *Salmonella enterica typhimurium* SipD using ClustalW (29) and with BipD by structure superposition. The sequence alignment was submitted to the ESPript server (30) for graphical representation.

Limited Proteolysis—Pure IpaD at 1 mg/ml was incubated with sequencing grade trypsin (Promega) in 20 mM Tris, pH 7.5, 150 mM NaCl. Ratios of trypsin:IpaD (w/w) of 1:50, 1:100, 1:200, 1:500 and 1:5000 were prepared and incubated in a water bath at 37 °C for 1 h. The reaction was stopped by the addition of 2× SDS-PAGE sample buffer followed by boiling for 5 min. The samples were analyzed by SDS-PAGE and sent for N-terminal

sequencing (Protein Characterization Facility, Department of Biochemistry, University of Oxford).

The broad-spectrum serine protease subtilisin Carlsberg from *Bacillus licheniformis* (Sigma) was added to IpaD in a 1:5000 (w/w) ratio (enzyme:protein) and incubated at 20 °C for 72 h to mimic the conditions under which crystals grew. The digested protein was then applied to a Superdex 200 (HR 10/30) column (GE Biosciences) equilibrated in 20 mM Tris, pH 7.5, 100 mM NaCl, 10 mM dithiothreitol. Undigested IpaD was applied to the same column under identical conditions.

Tip Localization of IpaD/BipD/IpaB and Hemolysis Assay—S. flexneri were grown to log phase in tryptic soy broth according to established protocols (31). Bacteria were fixed to glass slides or carbon/Formvar-coated copper grids. Monoclonal anti-IpaD, rabbit anti-BipD, or rabbit anti-IpaB IgG was used to detect IpaD (11), BipD, or IpaB (supplemental Fig. 2), respectively. Alexa Fluor 488 goat anti-mouse IgG or Alexa Fluor 568 goat anti-rabbit IgG was used to detect the primary antibody for confocal microscopy, while gold-labeled goat anti-mouse IgG or anti-rabbit IgG was used for electron microscopy. Hemolysis assays were performed as described in Ref. 4.

RESULTS

Structure of IpaD and BipD—The structure of *S. flexneri* IpaD was determined at 3.0 Å by SIRAS, using a selenomethionine derivative and cross-crystal averaging between various crystal forms (18) (Table 1). The electron density (Fig. 2*a*) allowed building of a model for IpaD residues 39–322 (Figs. 1*a* and 2*b*). The structure of *B. pseudomallei* BipD was determined at 2.8 Å by MIRAS using K_2PtCl_4 and SeMet derivatives (27) (Table 1). The electron density (Fig. 2*c*) allowed construction of a model from residues 35–111 and 127–301 (Figs. 1*c* and 2*d*).

Despite sharing only 26% identity at the sequence level, the structures of IpaD and BipD are highly homologous (r.m.s.d. = 1.6 Å over 161/283 Cα atoms). Both proteins are characterized

FIGURE 2. **Stereo views of IpaD and BipD electron density (*a* and *c*) and main chain traces (*b* and *d*) are shown.** The electron density is calculated with coefficients $2F_o - wF_c$ and phases derived from the final models. The IpaD density in *a* is contoured at 1.0 σ around residues 284–304 in the C-terminal coiled-coil helix and the BipD density in *c* around residues 154–172 in the N-terminal coiled-coil helix. *b* and *d* show complete main chain traces oriented so that the N and C termini are at the *bottom* of the picture.

by a long helical coiled-coil formed between a helix at the center of the sequence and a helix at the C terminus (Fig. 1*b*). A predominantly helical domain (hereafter termed the N-terminal domain)
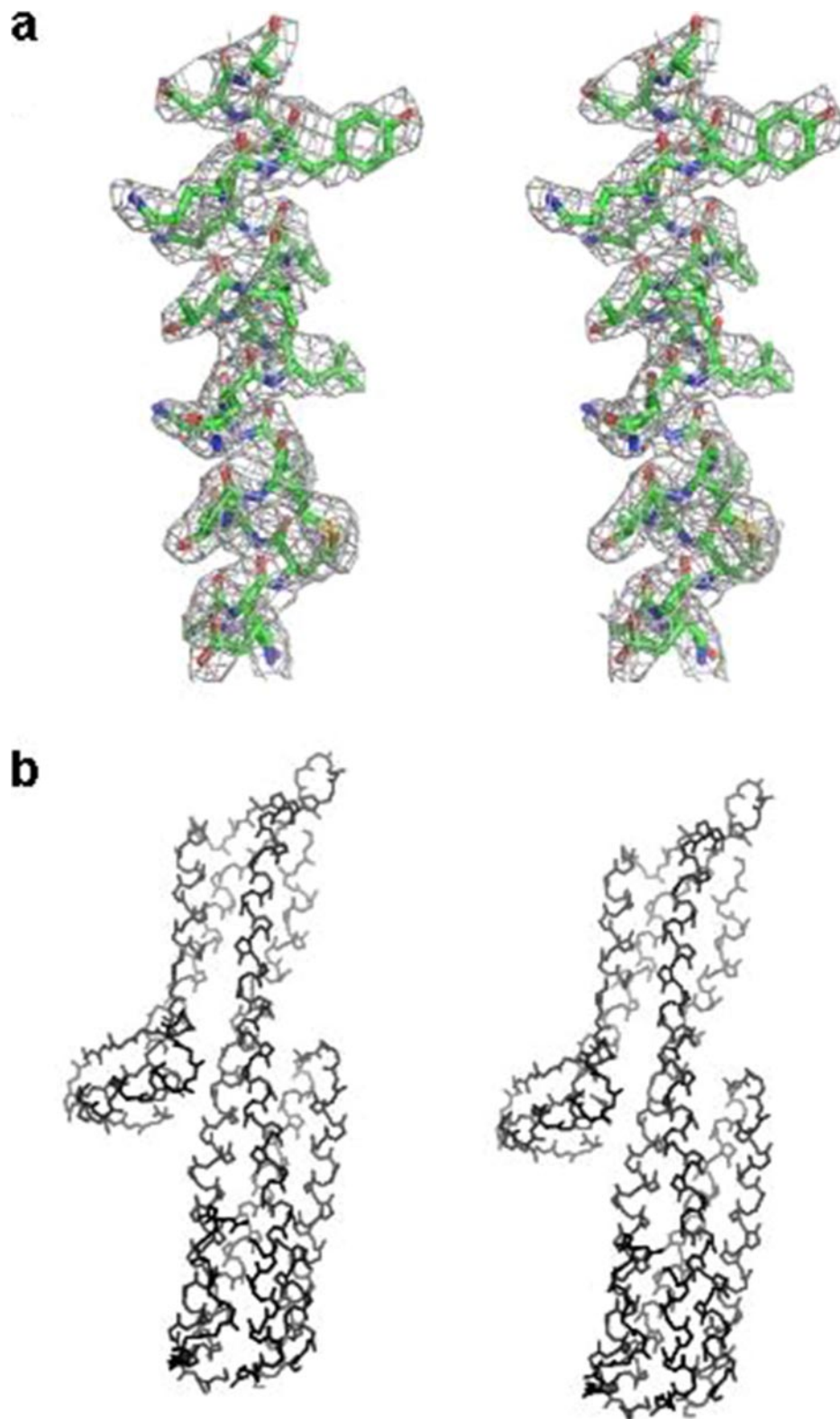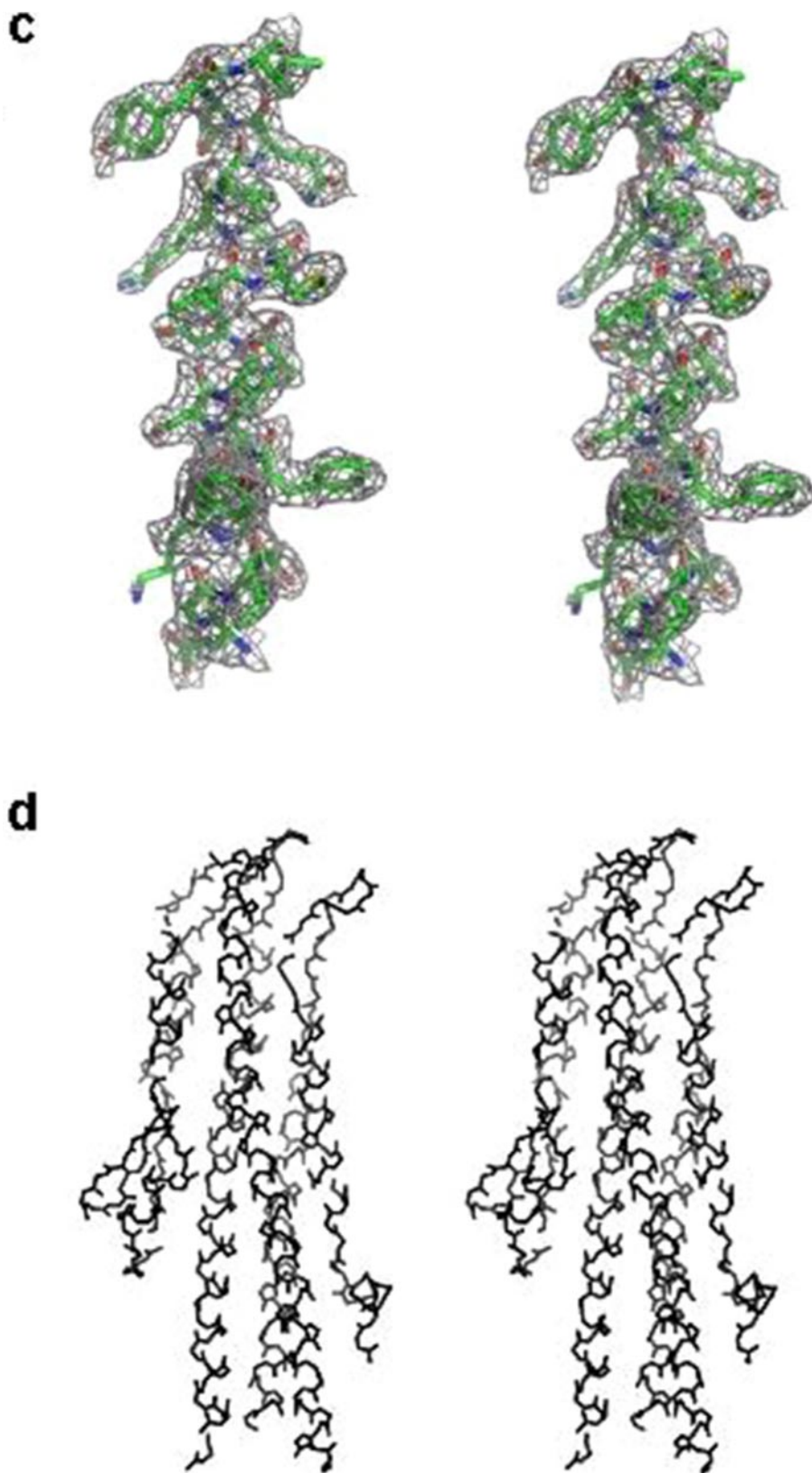
FIGURE 2—*continued*

the coiled-coil. Two helices from the N-terminal domain (named $\alpha1$ and $\alpha2$, see Fig. 1*b*) fold against one end of the coiled-coil, while two helices from the C-terminal domain ($\alpha4$ and $\alpha6$) pack against the other end of the coil. Both molecules therefore comprise two four-helix bundles that share the long coiled-coil. In addition, the N-terminal domain of IpaD contains a helical insertion relative to BipD between $\alpha2$ and $\alpha3$, which wraps around the end of the coiled-coil, while BipD contains a less structured insertion relative to IpaD between $\alpha1$ and $\alpha2$. In both IpaD and BipD, the C-terminal domain is embellished by a three-stranded anti-parallel β-sheet at the very end of the coil and an insertion of a short α-helix ($\alpha5$) and two β-strands (βC, βD) between $\alpha4$ and $\alpha6$ of the bundle. Despite the conserved topology, the relative orientation of $\alpha5$-βC-βD compared with the rest of the molecule differs between IpaD and BipD. The C-terminal residues are not visible in any of the structures. These are the residues that have been demonstrated to be essential for binding of IpaD to the tip of the *S. flexneri* needle (11). Disordered termini have been observed in other T3SS (32) and flagellar filament (33) molecules and this feature has been proposed to be important in correct assembly of these structures (33).

N-terminal Domain as Chaperone—The N-terminal four-helix bundle of IpaD/BipD shows strong structural homology with chaperones of T3SS filament-forming proteins (DALI (28)). The strongest hit (Z-score = 11.0) is the flagella chaperone FliS (Fig. 3*a*), a four-helix bundle that prevents premature assembly of the flagellum by binding the C-terminal helix of FliC (34). A DALI search using the N-terminal domain of IpaD alone retrieved YscE (35), the putative chaperone of the *Y. pestis* needle component YscF (Fig. 3*b*). In addition, the structure of CesA, the chaperone of EspA (a protein which forms a helical filament extension to the T3SS needle of enteropathogenic *Escherichia coli*) is also reminiscent of the IpaD/BipD N-terminal domain (32).

precedes the first helix of the central coiled-coil, while the sequence encoding a mixed α-β domain (hereafter termed the C-terminal domain) is inserted between the two long helices of

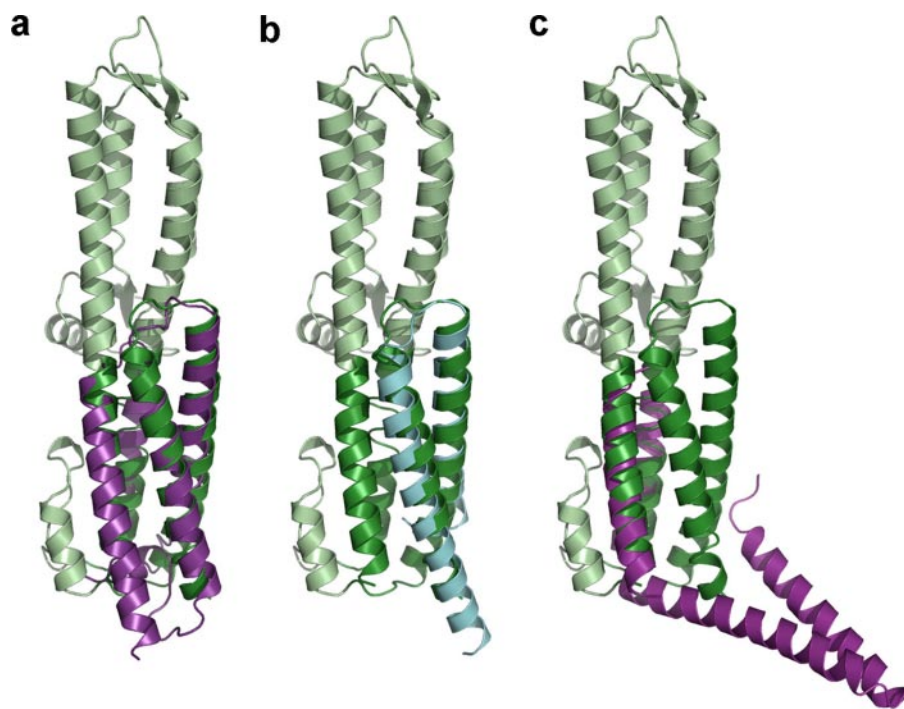# Self-chaperoning of the T3SS Needle Tip Proteins IpaD and BipD

FIGURE 3. **The N-terminal domain is a chaperone.** *a*, *ribbon diagram* of IpaD (*green*) superposed on *Aquifex aeolicus* FliS (*purple*, 1ORJ-A (r.m.s.d. = 2.0 Å over 103 Cα atoms) (39). *b*, *ribbon diagram* of IpaD (*green*) superposed on *Y. pestis* YscE (*light blue*, 1ZW0-A, r.m.s.d. = 1.8 Å over 57 Cα atoms) (35). *c*, *ribbon diagram* of IpaD (*green*) superposed on *Bacillus subtilis* FliS (*purple*, 1VH6) demonstrating the opened four-helix bundle.

the N-terminal domain, the coiled-coil is rigid and invariant between the two crystallographically independent molecules in the intact IpaD crystals and the three independent molecules seen in the BipD crystals. In the absence of the N-domain, however, the coiled-coil acquires flexibility, as demonstrated in the four crystallographically independent truncated IpaD molecules. These results represent the first examples of T3SS molecules self-chaperoning.

IpaD/BipD and Actin Reprogramming—Three of the top five hits against the DALI data base using IpaD/BipD as a search model are proteins involved in rearrangements of the actin cytoskeleton; talin (38) (Z-score = 10.8, r.m.s.d. = 2.2 Å over 111 Cα atoms), vinculin (39) (Z-score = 10.1, r.m.s.d. = 2.3 Å over 106 Cα atoms) and α-catenin (40) (Z-score = 9.0, r.m.s.d. = 3.9 Å over 158 Cα atoms) (supplemental Fig. 1). Furthermore, like IpaD/BipD, these structural homologues are proteins that are characterized by multiple helical bundles which are capable of helical rearrangement. This is significant as bacteria of the *Shigella/Salmonella* family cause membrane ruffling by actin re-arrangement to invade non-phagocytic cells. A possible role for IpaD/BipD in interfering with host cell actin is examined under "Discussion."

IpaD/BipD at the Tip of the Needle—We have recently proposed a model by which LcrV, the functional homologue of IpaD/BipD in *Y. pestis*, may oligomerize at the tip of the needle based on homologies between the LcrV and MxiH structures (16). However, although we can immunolabel IpaD on the tip of the *S. flexneri* needle (11), we have been unable to directly visualize a *S. flexneri* tip complex. This is not surprising as modeling of IpaD/BipD onto the needle in an analogous way to the LcrV results in a structure that would be difficult to visualize at the resolution of our current images, appearing as an extension to the needle, compared with the more bulky LcrV tip (data not shown).

Despite this, one of the IpaD crystal structures (CF-2) does point toward a possible arrangement of IpaD/BipD at the tip. The crystal, which diffracted to 2.1 Å, contains a tightly packed dimer (Fig. 5a) in which the two copies of the molecule in the asymmetric unit are related by a rotation of 72.2° around the long axis of the molecule and a rise of 4.6 Å, comparable with the parameters defining the 1-start helix of the MxiH needle (16). This dimer buries 1500 Å² (14%) of the solvent-accessible surface area of each IpaD monomer (37), including the hydrophobic strip that runs along the length of the coiled-coil, and contains two inter-molecular salt bridges (Lys-151-Glu-229

During the initial crystallization trials of IpaD we observed a crystal form which grew over a long period of time that was shown by N-terminal sequencing to consist of a truncated form of the protein (18). Incubation of IpaD with increasing concentrations of trypsin resulted in a gradual degradation to a protease resistant core (Fig. 4a) identified by N-terminal sequencing to start at Ile138. The proteolytic sensitivity of the N-terminal domain of IpaD is in agreement with our earlier biophysical characterization of IpaD which demonstrated that the N-terminal domain unfolds at lower temperatures and independently of the rest of the molecule (36).

To date, no specific chaperones for IpaD or BipD have been identified. Our data suggest that the role of the N-terminal domain of IpaD/BipD is to chaperone residues on the coiled-coil involved in interactions with the needle and/or itself. Removal of the N-terminal domain *in silico* results in the exposure of 2100 Å² of solvent-accessible surface area (37), including a hydrophobic strip that runs along the face of the two α-helices of the coiled-coil (Fig. 4b). Removal of the N-terminal domain of BipD exposes an even more extended patch (2300 Å²). All crystals grown with N-terminally truncated IpaD pack in such a way as to bury this patch in crystal contacts. Furthermore, proteolytic removal of the N-terminal domain of IpaD leads to oligomerization in solution. Full-length IpaD elutes as an ~50-kDa protein during size exclusion chromatography (Fig. 4c). Subtilisin treatment, which clips the N-terminal third of the molecule (18), leads the truncated form to elute as an ~115-kDa protein, a size consistent with the formation of a tetramer or pentamer.

In addition, the helices of the coiled-coil seem to be constrained by the N-terminal domain (Fig. 4d). In the presence of
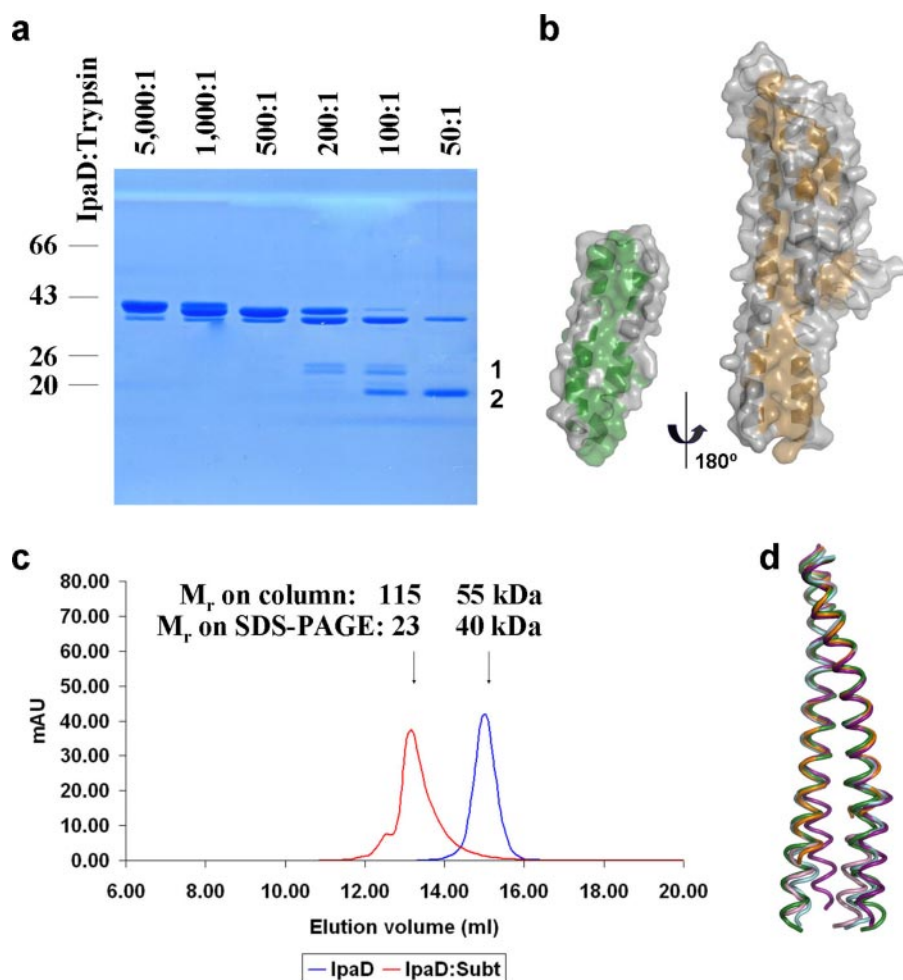
FIGURE 4. **Consequences of removal of the N-terminal domain.** *a*, proteolytic sensitivity of the N-terminal domain of IpaD. IpaD was incubated with trypsin at various ratios (w:w), and the resulting digests were resolved on SDS-PAGE. Band 1 (24 kDa) begins at residue 120 and Band 2 (20 kDa) at residue 138. *b*, surface representation of IpaD$_{39-130}$ (*left*) and IpaD$_{131-322}$ (*right*) with hydrophobic residues colored *green* and *brown*, respectively. IpaD$_{39-130}$ is rotated through 180° along the long axis relative to IpaD$_{131-322}$ to demonstrate the complementary hydrophobic surfaces. The surface is presented as transparent to allow visualization of the secondary structure. *c*, analytical gel filtration chromatography (Superdex 200, HR 10/30) of IpaD before and after subtilisin treatment. Elution volume of each species is noted along with the M_r calculated from SDS-PAGE. *d*, overlay of five structures of the IpaD coiled-coil demonstrating the flexibility of the helices in the absence of the N-terminal domain. The conformation of the coil in the presence of the N-terminal domain is shown in *green*. The C-terminal domain has been removed to aid clarity.

tion (K151E; E154K) reduces the hemolytic activity to 55.3 ± 3.6% of that of the wild type bacteria.

One major consequence of the formation of this pentamer is the fact that it is closed, *i.e.* there is no hole through the center of the structure. This is consistent with the earlier observations that bacteria lacking IpaD secrete the later effector proteins constitutively (3). However, the observation in the same study that bacteria lacking IpaB display the same phenotype, combined with data showing surface localization of IpaB (41), led to the proposal that IpaD and IpaB form a plug together in the needle (3). Subsequent studies have demonstrated IpaB decorates the surface of *S. flexneri* in a punctate pattern (42) and is associated with the tips of purified needles.[9],[10] Although there is currently no atomic model of IpaB, it is predicted to contain two long coiled-coil regions, the first from residues 130–170 and the second at the extreme C terminus (residues 530–580) (43). We predict that IpaB has a similar fold to IpaD/BipD, with an internal coiled-coil but with a much larger C-terminal domain. Due to the helical rise of the pentamer, the interface between the fifth and the first molecule is different to that between the other consecutive pairs of monomers, and therefore it is possible that the final position of the pentamer is filled by IpaB. This would explain the need for both IpaD and IpaB to properly control

and Glu-154-Lys-300) involving residues that are solvent exposed in the full-length monomer.

The residues involved in forming this contact are clustered in the C-terminal helix, with one face providing half of the binding pocket for another face of the same helix from a neighboring monomer (Fig. 5*b*). These residues are the most conserved residues in the *Shigella/Salmonella* family of tip proteins (Fig. 1*d*). By superposing molecule A onto molecule B, and then again in an iterative fashion, it is possible to build a tightly packed pentamer, which buries all of the hydrophobic surfaces in the molecule (Fig. 5*c*). This pentamer buries 3000 Å^2 (28%) of the solvent-accessible surface area of each monomer. Furthermore, the arrangement places the N-terminal helix of the coiled-coil on the outside of the pentamer, thereby allowing the N-domain to be positioned outside of the needle. Supporting the physiological relevance of these interactions, a double mutation that destroys the two salt bridges involved in the pentamer forma-

secretion, with four copies of IpaD polymerizing at the tip of the needle and one molecule of IpaB locking the structure.

To test this hypothesis, we first investigated the presence of IpaD and IpaB at the tip of the needle. Using a variety of techniques, including immunofluorescence (supplemental Fig. 2) and electron microscopy (data not shown), we were able to observe both IpaD and IpaB at the surface of wild type *S. flexneri* (Table 2). Surface-localized IpaB was dependent on the presence of IpaD (Table 2), while IpaD was still surface-localized in the absence of IpaB (11). This suggests that IpaD is able to directly bind the MxiH needle, while IpaB requires a binding surface that involved residues on IpaD.

Based on the structure of the IpaD monomer, we designed mutants to cleanly remove the N-terminal (41–130) and C-ter-
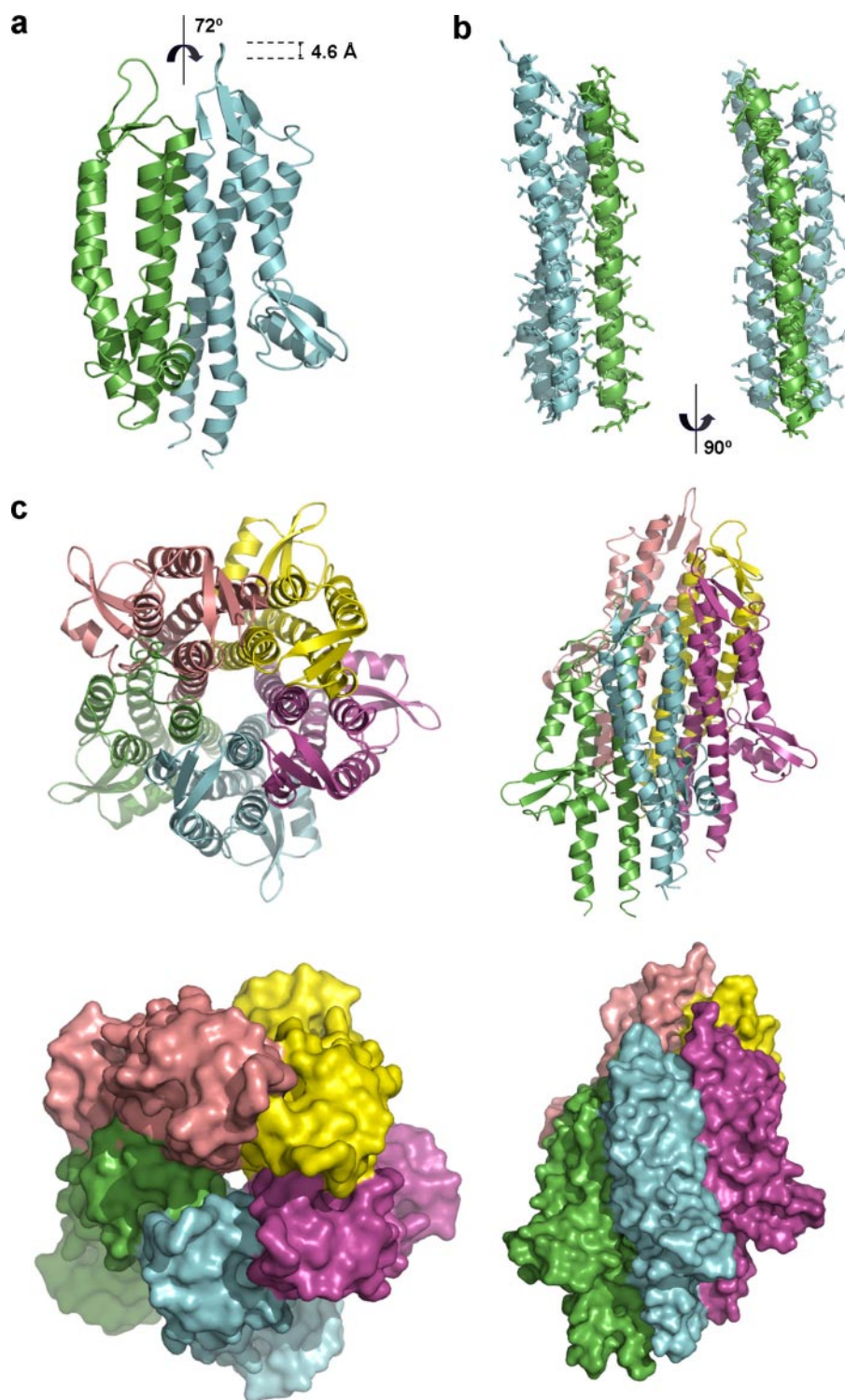

FIGURE 5. **Oligomerization of IpaD.** *a*, *ribbon diagram* of the non-crystallographic dimer found in crystal form 2 (18). Molecule A is shown in *green* and molecule B in *blue*. *b*, detailed view of the dimer interaction site with side chains displayed, colored as in *a*. Only structural elements that contribute to the binding site are displayed for clarity. *c*, pentamer produced using the non-crystallographic symmetry from crystal form 2. At the *top* are *ribbon* representations and at the *bottom* surface views. The *panels* on the *left* are related to the *panels* on the *right* by a rotation of 90°.

minal (192–267) domains and assessed their ability to complement an *ipaD*⁻ mutant. Removal of the N-terminal domain did not affect the binding of either IpaD or IpaB at the tip of the needle, consistent with its role as a chaperone. Removal of the C-terminal domain, on the other hand, completely abolished binding of IpaB at the tip, without affecting localization of IpaD (Table 2). This is consistent with the hetero-pentamer model proposed, as the C-terminal domain of IpaD does not contribute significantly to the IpaD-IpaD interaction (as assessed using the MSDpisa server (37)). In contrast, it would likely be involved in binding of the much larger IpaB molecule. The result, therefore, highlights an essential role for the IpaD C-terminal domain in binding the IpaB molecule. In further support of this, BipD could also be visualized on the surface of *S. flexneri* when expressed in an *ipaD*⁻ mutant, but IpaB was unable to bind (Table 2).

DISCUSSION

Here we present the first structures of T3SS needle tip proteins from the *Shigella/Salmonella* family, which trigger uptake of the bacteria by non-phagocytic cells. The structures of IpaD and BipD, from *S. flexneri* and *B. pseudomallei*, respectively, are homologous, consisting of a central coiled-coil with a domain at either end. The structures demonstrate the first examples of self-chaperoning within T3SS molecules and have allowed us to construct a model for a needle tip complex of *S. flexneri*. Furthermore, we have been able to attribute different functions to distinct domains within the proteins.

IpaD has recently been shown to exist at the tip of the MxiH needle (11), from where it appears to orchestrate the correct insertion of

TABLE 2
Needle-tip localization of IpaD and IpaB

	Wild type	IpaD⁻	ipaD⁻/IpaD$_{\Delta 41-130}$	IpaD⁻/IpaD$_{\Delta 192-267}$	ipaD⁻/BipD
IpaD/BipD at needle-tip	+	−	+	+	+
IpaB at needle-tip	+	−	+	−	−

the IpaB/C translocon into host cell membranes (9). The structures of two other needle tip proteins from distinct T3SS families are known: LcrV from *Y. pestis* (17) and EspA from enteropathogenic *E. coli* (32). Both of these molecules also contain a central coiled-coil, but in other aspects there are few structural similarities with IpaD/BipD, especially at the N terminus of the molecules. These structures, combined with our recent needle subunit structure (16) and the structures of the polymerizing components of the bacterial flagellum (44), serve to highlight the importance of intramolecular helical coiled-coils as scaffolds for superhelical assemblies while emphasizing that specific functions can be "bolted onto" the assembly in the form of structurally distinct domains.

Most T3SS proteins are chaperone-bound within the bacterial cytoplasm. Chaperones are thought to play multiple roles both in directing T3SS proteins to the base of the apparatus for export and also in preventing premature assembly of structural components (45). For example, EspA interacts with CesA in the bacterial cytoplasm, while LcrV seems to be chaperoned by LcrG since expression of LcrV in the absence of LcrG leads to oligomerization of LcrV (46). Although no structure of LcrG is available, the protein is predicted to be α-helical and to interact with the central coiled-coil of LcrV with 1:1 stoichiometry (46).

Based on our structural and biochemical data, we propose that the most complete models of IpaD and BipD found in our crystals represent the form of the molecule present in the bacterial cytoplasm and that the role of the N-terminal domain is to chaperone residues on the coiled-coil involved in interactions at the tip of the needle. The proteins would be partially unfolded during export through the needle (16) and would refold at tip of the needle into an alternate conformation with the N-terminal domain pointing away from the coiled-coil. This would require that the interactions formed at the tip of the needle are more favorable than the interactions between the N-terminal domain and the coiled-coil. In this context, it is noteworthy that two structures for FliS, the closest IpaD/BipD structural homologue, have been determined that are related by opening of the four-helix bundle and rotation of one pair of helices with respect to the other (1ORJ and 1VH6) (Fig. 3*c*).

Removal of the N-terminal domain of IpaD by proteolysis also resulted in increased flexibility of the coiled-coil. Such flexibility of the coiled-coil appears to be a common feature of needle and tip proteins and may be of importance in signaling. Our MxiH crystal structure revealed two conformations of the molecule, related by a hinging motion part way down the coiled-coil (16), while LcrV has a significant kink in its C-terminal helix (17), which matches the kink in one of the MxiH conformations. EspA, on the other hand, contains a straight coiled-coil, as seen when it was crystallized bound to its chaperone, which would likely limit the flexibility of the helices (32). By removing the N-terminal domain of IpaD we appear to have crystallographically trapped the coiled-coil in a number of states between the extremes of LcrV and EspA.

The IpaD and BipD structures represent the first examples of self-chaperoning T3SS molecules. A major question, therefore, is why they have adopted the strategy of incorporation of the chaperone into the polypeptide chain, while other T3SS filament-forming proteins maintain separate chaperones. It is

tempting to speculate that fusion of the chaperone to the rest of the molecule allows for greater flexibility of function within a single polypeptide chain. Intriguingly, given the mechanism of infection employed by the *Shigella*/*Salmonella* family, three of the top five structural homologues of the N-terminal half of IpaD/BipD are proteins involved in the re-arrangement of the actin cytoskeleton. Given that *S. flexneri* secretes large amounts of IpaD upon activation, significant quantities may translocate into the host cell cytoplasm, where it would be free to refold into the bacterial cytoplasmic form and co-operate with other effector molecules in the re-programming of the cytoskeleton. It is worth noting that a domain of SipA, an actin-binding *Salmonella* effector molecule homologous to IpaA is also a structural homologue of vinculin (47), while a recent crystal structure of vinculin bound to a helix of IpaA has demonstrated that *S. flexneri* effectors do indeed utilize molecular mimicry during infection (48).

The key role for IpaD occurs at the tip of the needle, where it is essential for mediating correct insertion of the IpaB/IpaC translocon into host cell membranes (9, 11). We propose a model for an IpaD/IpaB hetero-pentamer at the tip of the MxiH needle, based on crystal contacts in one of the crystal forms. This model involves export of four copies of IpaD to the tip of the needle, where they pack into the needle via the C-terminal residues. Finally, a copy of IpaB slots into the pentamer via its central coiled-coil, thereby locking the pentamer and preventing further secretion of other effectors. This model is consistent with the helical parameters of the MxiH needle and with the published null mutant phenotypes of *S. flexneri* (8). Mutations designed based on the structure of IpaD are wholly consistent with the model and demonstrate that the C-terminal domain of IpaD is critical for binding of IpaB at the needle tip. The small amounts of effector proteins secreted in the absence of activation, termed "leakage," could be explained by needles that have not fully assembled the IpaD/IpaB plug, by premature loss of IpaD/IpaB from the tip, or by a "breathing" of the structure between a closed and open state. In addition to closing the needle, this model would also position the predicted large C-terminal domain of IpaB as the most distal point from the needle and therefore the likely point of contact with the host cell. The C-terminal domain of IpaB contains two predicted trans-membrane helices and, significantly, the top hit when searching the Protein Data Bank with its sequence (FFAS Server (49)) is Colicin B, a bacterial pore-forming toxin, which utilizes a helical trans-membrane hairpin (50). Activation of the tip complex, by contact with the host cell, could trigger a conformational change leading to an opening of the pentamer, possibly into a conformation more similar to our earlier model of LcrV at the tip (16). This would open the channel to allow export and assembly of the pore components IpaB and IpaC into the host cell membrane, thereby triggering the infectious process.

Self-chaperoning of the T3SS Needle Tip Proteins IpaD and BipD

Note Added in Proof—The structure for another crystal form of BipD has recently been published (Erskine, P. T., Knight, M. J., Ruaux, A., Mikolajek, H., Wong Fat Sang, N., Withers, J., Gill, R., Wood, S. P., Wood, M., Fox, G. C., and Cooper, J. B. (2006) *J. Mol. Biol.* **363,** 125–136). The structure revealed is consistent with those presented herein. The authors do not discuss a role for BipD at the tip of the T3SS needle; however, they propose that their crystallographic dimer has biological relevance. Their dimer is not observed in any of our IpaD or BipD crystals and is constructed from a head-to-tail arrangement (incompatible with assembly at the tip of the needle). Our model for IpaD at the tip is also supported by recent 2D projection images of IpaD at the Shigella needle tip (Sani, M., Botteaux, A., Parsot, C., Sansonetti, P., Boekema, E. J., and Allaoui, A. (2006) *Biochem. Biophys. Acta* doi:10.1016/j.bbagen.2006.10.007).

REFERENCES

1. Kotloff, K. L., Winickoff, J. P., Ivanoff, B., Clemens, J. D., Swerdlow, D. L., Sansonetti, P. J., Adak, G. K., and Levine, M. M. (1999) *Bull W. H. O.* **77,** 651–666
2. Blocker, A., Jouihri, N., Larquet, E., Gounon, P., Ebel, F., Parsot, C., Sansonetti, P., and Allaoui, A. (2001) *Mol. Microbiol.* **39,** 652–663
3. Menard, R., Sansonetti, P., and Parsot, C. (1994) *EMBO J.* **13,** 5293–5302
4. Blocker, A., Gounon, P., Larquet, E., Niebuhr, K., Cabiaux, V., Parsot, C., and Sansonetti, P. (1999) *J. Cell Biol.* **147,** 683–693
5. Johnson, S., Deane, J. E., and Lea, S. M. (2005) *Curr. Opin. Struct. Biol.* **15,** 700–707
6. He, S. Y., Nomura, K., and Whittam, T. S. (2004) *Biochim Biophys. Acta* **1694,** 181–206
7. Cossart, P., and Sansonetti, P. J. (2004) *Science* **304,** 242–248
8. Menard, R., Sansonetti, P. J., and Parsot, C. (1993) *J. Bacteriol.* **175,** 5899–5906
9. Picking, W. L., Nishioka, H., Hearn, P. D., Baxter, M. A., Harrington, A. T., Blocker, A., and Picking, W. D. (2005) *Infect Immun.* **73,** 1432–1440
10. Blocker, A., Komoriya, K., and Aizawa, S. (2003) *Proc. Natl. Acad. Sci. U. S. A.* **100,** 3027–3030
11. Espina, M., Olive, A. J., Kenjale, R., Moore, D. S., Ausar, S. F., Kaminski, R. W., Oaks, E. V., Middaugh, C. R., Picking, W. D., and Picking, W. L. (2006) *Infect Immun.* **74,** 4391–4400
12. Mueller, C. A., Broz, P., Muller, S. A., Ringler, P., Erne-Brand, F., Sorg, I., Kuhn, M., Engel, A., and Cornelis, G. R. (2005) *Science* **310,** 674–676
13. White, N. J. (2003) *Lancet* **361,** 1715–1722
14. Stevens, M. P., Haque, A., Atkins, T., Hill, J., Wood, M. W., Easton, A., Nelson, M., Underwood-Fowler, C., Titball, R. W., Bancroft, G. J., and Galyov, E. E. (2004) *Microbiology* **150,** 2669–2676
15. Cordes, F. S., Komoriya, K., Larquet, E., Yang, S., Egelman, E. H., Blocker, A., and Lea, S. M. (2003) *J. Biol. Chem.* **278,** 17103–17107
16. Deane, J. E., Roversi, P., Cordes, F. S., Johnson, S., Kenjale, R., Daniell, S., Booy, F., Picking, W. D., Picking, W. L., Blocker, A. J., and Lea, S. M. (2006) *Proc. Natl. Acad. Sci. U. S. A.* **103,** 12529–12533
17. Derewenda, U., Mateja, A., Devedjiev, Y., Routzahn, K. M., Evdokimov, A. G., Derewenda, Z. S., and Waugh, D. S. (2004) *Structure (Camb.)* **12,** 301–306
18. Johnson, S., Roversi, P., Espina, M., Deane, J. E., Birket, S., Picking, W. D., Blocker, A., Picking, W. L., and Lea, S. M. (2006) *Acta Crystallogr. Sect. F Struct. Biol. Crystallogr. Commun.* **62,** 865–868
19. Schneider, T. R., and Sheldrick, G. M. (2002) *Acta Crystallogr. Sect. D Biol. Crystallogr* **58,** 1772–1779
20. Vonrhein, C., Blanc, E., Roversi, P., and Bricogne, G. (2005) in *Crystallographic Methods* (Doublie, S., ed) Humana Press, Totowa, NJ
21. de La Fortelle, E., and Bricogne, G. (1997) *Methods Enzymol.* **276,** 472–494
22. Terwilliger, T. C. (2003) *Methods Enzymol.* **374,** 22–37
23. CCP4. (1994) *Acta Crystallogr. Sect. D Biol. Crystallogr.* **50,** 760–763
24. McRee, D. E. (1999) *J. Struct. Biol.* **125,** 156–165
25. Blanc, E., Roversi, P., Vonrhein, C., Flensburg, C., Lea, S. M., and Bricogne, G. (2004) *Acta Crystallogr. D Biol. Crystallogr.* **60,** 2210–2221
26. DeLano, W. L. (2002) The PyMOL Molecular Graphics System, DeLano Scientific, San Carlos, CA
27. Roversi, P., Johnson, S., Field, T., Deane, J. E., Galyov, E. E., and Lea, S. M. (2006) *Acta Crystallograph Sect. F Struct. Biol. Crystallogr. Commun.* **62,** 861–864
28. Holm, L., and Sander, C. (1993) *J. Mol. Biol.* **233,** 123–138
29. Thompson, J. D., Higgins, D. G., and Gibson, T. J. (1994) *Nucleic Acids Res.* **22,** 4673–4680
30. Gouet, P., Courcelle, E., Stuart, D. I., and Metoz, F. (1999) *Bioinformatics* **15,** 305–308
31. Pope, L. M., Reed, K. E., and Payne, S. M. (1995) *Infect. Immun.* **63,** 3642–3648
32. Yip, C. K., Finlay, B. B., and Strynadka, N. C. (2005) *Nat. Struct. Mol. Biol.* **12,** 75–81
33. Aizawa, S. I., Vonderviszt, F., Ishima, R., and Akasaka, K. (1990) *J. Mol. Biol.* **211,** 673–677
34. Evdokimov, A. G., Phan, J., Tropea, J. E., Routzahn, K. M., Peters, H. K., Pokross, M., and Waugh, D. S. (2003) *Nat. Struct. Biol.* **10,** 789–793
35. Phan, J., Austin, B. P., and Waugh, D. S. (2005) *Protein Sci.* **14,** 2759–2763
36. Espina, M., Ausar, S. F., Middaugh, C. R., Picking, W. D., and Picking, W. L. (2006) *Biochemistry* **45,** 9219–9227
37. Krissinel, E., and Henrick, K. (2005) in *Lecture Notes in Computer Science* (Berthold, M. R., ed) Springer, Berlin
38. Papagrigoriou, E., Gingras, A. R., Barsukov, I. L., Bate, N., Fillingham, I. J., Patel, B., Frank, R., Ziegler, W. H., Roberts, G. C., Critchley, D. R., and Emsley, J. (2004) *EMBO J.* **23,** 2942–2951
39. Izard, T., Evans, G., Borgon, R. A., Rush, C. L., Bricogne, G., and Bois, P. R. (2004) *Nature* **427,** 171–175
40. Pokutta, S., and Weis, W. I. (2000) *Mol. Cell.* **5,** 533–543
41. Venkatesan, M. M., Buysse, J. M., and Oaks, E. V. (1992) *J. Bacteriol.* **174,** 1990–2001
42. West, N. P., Sansonetti, P., Mounier, J., Exley, R. M., Parsot, C., Guadagnini, S., Prevost, M. C., Prochnicka-Chalufour, A., Delepierre, M., Tanguy, M., and Tang, C. M. (2005) *Science* **307,** 1313–1317
43. Lupas, A. (1996) *Methods Enzymol.* **266,** 513–521
44. Yonekura, K., Maki-Yonekura, S., and Namba, K. (2003) *Nature* **424,** 643–650
45. Parsot, C., Hamiaux, C., and Page, A. L. (2003) *Curr. Opin. Microbiol* **6,** 7–14
46. Lawton, D. G., Longstaff, C., Wallace, B. A., Hill, J., Leary, S. E., Titball, R. W., and Brown, K. A. (2002) *J. Biol. Chem.* **277,** 38714–38722
47. Lilic, M., Vujanac, M., and Stebbins, C. E. (2006) *Mol. Cell.* **21,** 653–664
48. Hamiaux, C., van Eerde, A., Parsot, C., Broos, J., and Dijkstra, B. W. (2006) *EMBO Rep.* **7,** 794–799
49. Jaroszewski, L., Rychlewski, L., Li, Z., Li, W., and Godzik, A. (2005) *Nucleic Acids Res.* **33,** W284–W288
50. Hilsenbeck, J. L., Park, H., Chen, G., Youn, B., Postle, K., and Kang, C. (2004) *Mol. Microbiol.* **51,** 711–720

Self-chaperoning of the Type III Secretion System needle tip proteins IpaD and BipD

Steven Johnson,[ab†] Pietro Roversi,[a†] Marianela Espina,[c] Andrew Olive,[c] Janet E. Deane,[a] Susan Birket,[c] Terry Field,[d] William D. Picking,[c] Ariel Blocker,[b] Edouard E. Galyov,[d] Wendy L. Picking[c] and Susan M. Lea[ba*]

[a]*Laboratory of Molecular Biophysics, Department of Biochemistry, University of Oxford, UK,* [b]*Sir William Dunn School of Pathology, University of Oxford, UK, and* [c]*Department of Molecular Biosciences, University of Kansas, USA.* [d]*Division of Microbiology, Institute for Animal Health, Compton Laboratory, Berkshire, RG20 7NN, UK. E-mail:* susan.lea@path.ox.ac.uk [†] These authors contributed equally to this work.

Supplementary Table 1. IpaD and BipD experimental phasing statistics (program SHARP)

Phasing		IpaD SIRAS		BipD MIRAS		
Dataset		Native	SeMet (pk)	Native	K_2PtCl_4	SeMet
Resolution (Å)		43.0-2.8	34.0-3.4	54.0-2.7	33.0-3.0	44.0-3.3
Wavelength (Å)		0.9757	0.9792	0.9330	0.9330	0.9794
Heavy atom sites		-	10 Se	-	2 Pt	10 Se
Phasing Power (iso)	Centrics	-	34.0-4.5 Å: 0.587 34.0-3.4 Å: 0.609	-	33.0-4.5 Å: 1.166 33.0-3.0 Å: 0.597	44-4.5 Å: 1.358 44-3.3 Å: 0.777
	Acentrics	-	34.0-4.5 Å: 0.365 34.0-3.4 Å: 0.458	-	33.0-4.5 Å: 1.061 33.0-3.0Å: 0.706	44-4.5 Å: 1.218 44-3.3 Å: 0.848
Phasing Power (ano)		-	34.0-4.5 Å: 2.210 34.0-3.4 Å: 2.064	-	33.0-4.5 Å: 1.803 33.0-3.0Å: 0.787	44-4.5 Å: 0.660 44-3.3 Å: 0.345
Acentrics FOM		34.0-4.5Å: 0.715 34.0-3.4 Å: 0.560		44-4.5 Å: 0.493 44-3.3 Å: 0.218		
Centrics FOM		34.0-4.5Å: 0.366 34.0-3.4 Å: 0.283		44-4.5 Å:0.438 44-3.3 Å:0.245		

Supplementary Figure 1. Structural homologies with actin-binding proteins. **(a)** Ribbon diagram of IpaD (green) overlayed on *Mus musculus* Talin residues 482-655 (yellow-orange, 1SJ7-A, rmsd = 2.2 Å over 111 Cα atoms). **(b)** Ribbon diagram of IpaD (green) overlayed on *Homo sapiens* Vinculin residues 1-258 (sand, 1RKC-A, rmsd = 2.3 Å over 106 Cα atoms). **(c)** Ribbon diagram of IpaD (green) overlayed on *Mus musculus* α-Catenin dimerization domain (pink, 1DOV-A, rmsd = 3.9 Å over 158 Cα atoms).

Supplementary Figure 2. Detection of IpaB on the surface of *Shigella flexneri* in a punctuate pattern using Immunofluorescence as described in the main text (*Methods*). **(a)** When an *ipaB* null mutant is treated with rabbit anti-IpaB antiserum/Alexa fluor 568-conjugated goat anti-rabbit IgG no IpaB is visualised on the cell surface **(b)** Whereas in the wild type cells the same treatment detects IpaB on the cell surface **(c)** and **(d)** Differential interference contrast micrograph of panels (a) and (b) respectively.
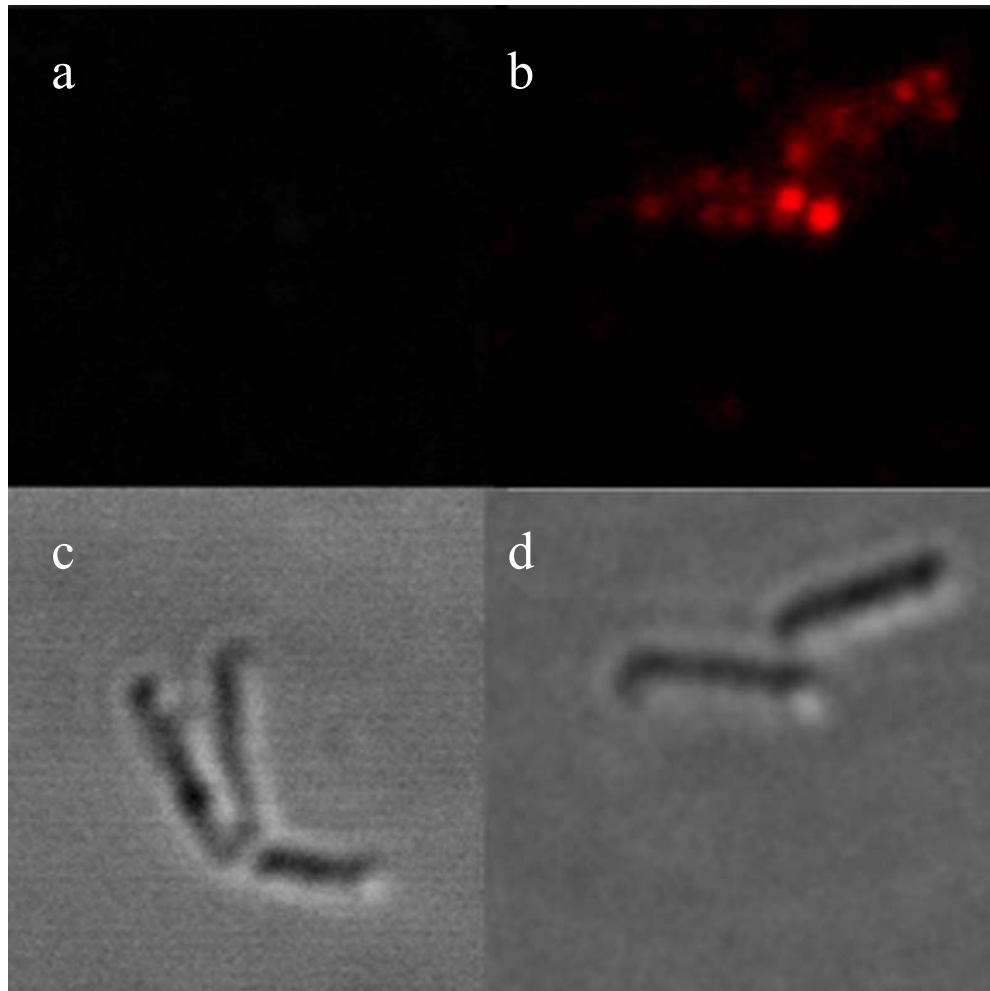
Supplementary Figure 1

Self-chaperoning of the Type III Secretion System Needle Tip Proteins IpaD and BipD

Steven Johnson, Pietro Roversi, Marianela Espina, Andrew Olive, Janet E. Deane,
Susan Birket, Terry Field, William D. Picking, Ariel J. Blocker, Edouard E. Galyov,
Wendy L. Picking and Susan M. Lea

Access the most updated version of this article at doi: 10.1074/jbc.M607945200

Alerts:
- When this article is cited
- When a correction for this article is posted

Click here to choose from all of JBC's e-mail alerts

Supplemental material:
http://www.jbc.org/content/suppl/2006/11/01/M607945200.DC1.html

This article cites 46 references, 16 of which can be accessed free at
http://www.jbc.org/content/282/6/4035.full.html#ref-list-1